SPECTRUM OF ENGINEERING SCIENCES
ISSN (E) 3007-3138 (P) 3007-312X VOLUME 4, ISSUE 3, 2026

SYNTHESIS AND CHARACTERIZATION OF ZNO/TIO$_2$ NANOPARTICLES: STRUCTURAL, OPTICAL, AND PHOTOCATALYTIC PROPERTIES

Shadab Azam[*1], Mahpara Abid[2], Syed Anam Shaheen Abbas Shah[3], Anam Shehzadi[4]

[*1,3]*Department of Physics University of Agriculture Faisalabad,Pakistan*
[2]*Department of Biotechnology Quaid I Azam University*
[4]*Department physics Government College University Faisalabad*

[*1]shadab.azam30@gmail.com, [2]islamabadmahparaabid97@gmail.com, [3]syedanamabbas123@gmail.com, [4]shehzadimurtaza385@gmail.com

DOI: https://doi.org/10.5281/zenodo.23615081

Keywords
ZnO nanoparticles; TiO_2 nanoparticles; ZnO/TiO_2 nanocomposite; heterojunction photocatalysis; charge separation; X-ray diffraction; optical band gap; photocatalytic dye degradation; wastewater treatment

Article History
Received: 01 January 2026
Accepted: 16 March 2026
Published: 31 March 2026

Copyright @Author
Corresponding Author: *
Shadab Azam

Abstract

Zinc oxide, titanium dioxide (TiO_2), and ZnO/TiO_2 nanocomposites were synthesised by a controlled chemical route, and their structural, optical, and photocatalytic properties were systematically characterised in order to establish a coherent structure–property–performance relationship. ZnO nanoparticles were prepared by a pH-controlled hydrothermal route, TiO_2 was obtained from a titanium alkoxide precursor and crystallised by calcination, and the composite was formed in situ by dispersing pre-formed ZnO in ethanol, adjusting the pH, and adding a titanium precursor before calcination at 500 °C for 2 h.

X-ray diffraction confirmed that the composite consisted of hexagonal wurtzite ZnO (JCPDS 36-1451) and anatase TiO_2 (JCPDS 21-1272) as separate phases, with no detectable impurity or zinc titanate phase; the crystallite size of the composite was smaller than that of pristine ZnO, consistent with the incorporation of TiO_2 within the ZnO matrix. Scanning electron microscopy and energy-dispersive X-ray spectroscopy provided the particle morphology, agglomeration behaviour, and elemental composition, while Fourier transform infrared spectroscopy confirmed the metal–oxygen bonding and Ti–O–Zn linkages of the composite.

Optical characterisation showed strong ultraviolet absorption, with the absorption edge of the composite displaced relative to the pristine oxides and the band gap decreasing from 3.48 eV for pure ZnO to 3.05 eV as the TiO_2 volume ratio increased; photoluminescence measurements indicated a change in emission intensity, interpreted in terms of charge-carrier recombination. The composite degraded the model organic dye more efficiently than either pristine oxide under identical conditions, and the kinetics followed a pseudo-first-order model. The enhancement is attributed to the staggered (type-II) band alignment at the ZnO/TiO_2 heterojunction, which spatially separates photogenerated electrons and holes, prolongs carrier lifetime, and improves interfacial charge transfer to adsorbed species.

The results establish a coherent structure property performance relationship and support the use of low-cost, chemically and thermally stable ZnO/TiO_2 nanocomposites for the removal of organic pollutants from contaminated water.

1. INTRODUCTION

Nanotechnology, the intentional design and manipulation of matter at a scale of order of 1 to 100 nm, has become one of the most prolific interdisciplinary research fields in the last three decades and engineered nanomaterials have laid the foundation of advances in energy conversion, environmental remediation, sensing, and medicine.

1.1 Introduction to Nanotechnology and Metal Oxide NPs

The defining feature of nanoscale materials is not just their small size, but the way those dimensions control behaviour. As particle dimensions decrease to nanometre dimensions, the surface to volume ratio increases sharply, density of surface defects and unsaturated bonds increases and quantum confinement starts to modify the electronic structure. The result is a class of materials with optical, electrical, thermal and catalytic properties that can be tuned by controlling size, shape, morphology and surface chemistry rather than by changing chemical composition alone. Metal oxide semiconductors are one of the most common nanomaterials because they have useful optoelectronic and catalytic properties, as well as chemical robustness, thermal stability, low cost, and relative non-toxicity. Typical members of this family are zinc oxide, titanium dioxide (TiO_2), tin dioxide (SnO_2), iron oxide (Fe_2O_3) and tungsten trioxide (WO_3). ZnO and TiO 2 are common in the photocatalysis literature, and the combination of these two materials into one composite architecture is the focus of the present investigation.

1.2 Properties and Uses of Zinc Oxide

Zinc oxide (ZnO) is an n-type II-VI semiconductor with a wide direct band gap (~3.37 eV at room temperature) and a large exciton binding energy (~60 meV) which allows efficient excitonic emission even at room temperature. It usually crystallises in the hexagonal wurzite structure and can be grown in a remarkable variety of morphologies – nanorods, nanowires, nanobelts, nanoflowers and quasi-spherical particles – depending on the synthesis route and growth conditions. ZnO has high electron mobility, strong ultraviolet absorption, high piezoelectric response, and excellent thermal and chemical stability. These properties are utilised in photocatalysis, ultraviolet photodetectors, gas sensors, dye-sensitized and perovskite solar cells, antibacterial coatings, transparent conductive films and piezoelectric energy harvesters. Its main drawbacks as a photocatalyst are the rapid recombination of photogenerated electron-hole pairs and photocorrosion in aqueous solution under prolonged ultraviolet light irradiation.

1.3 Properties and Applications of TiO2

Titanium dioxide is also an n-type semiconductor and exists mainly in three polymorphs: anatase, rutile and brookite. Anatase has been shown to be the most photocatalytically active form because of its higher surface area, higher density of surface hydroxyl groups and advantageous band-edge positions. The band gap of anatase is around 3.2 eV, whereas that of rutile is narrower, around 3.0 eV. TiO_2 is chemically inert, thermally stable, inexpensive, non-toxic, biocompatible and its photogenerated holes have strong oxidising potential. These properties have made it a standard material in environmental remediation, e.g., degradation of organic dyes and pollutants in water, air purification, self-cleaning and antifogging surfaces, photocatalytic hydrogen production by water splitting, and dye-sensitized solar cells. A practical downside of the same wide band gap that makes it stable is that it requires ultraviolet light for activation, which is a small fraction of the solar spectrum that reaches the Earth's surface (about 4–5%), and the photogenerated carriers recombine fast, thus limiting the quantum efficiency.

1.4 Advantages of ZnO/TiO 2 nanocomposite and synergistic effects

The combination of ZnO and TiO2 in a single nanocomposite is a well established strategy to overcome the limitations of each component. The two oxides have closely matched but offset band edge positions, and form a type-II (staggered) heterojunction. Under ultraviolet irradiation, photogenerated electrons from the conduction band of ZnO transfer to the conduction band of TiO2, and holes transfer from the valence band of TiO2 to the valence band of ZnO. This spatial separation of charge carriers reduces recombination, increases the

lifetime of the carriers, and increases the efficiency of interfacial charge transfer to adsorbed species, all contributing to a higher photocatalytic activity than either pristine oxide. The composite also shows an increased specific surface area and higher density of active sites at the heterointerface. However, note that the direction and extent of charge migration depends on the relative proportions of the two oxides and the character of the junction; some configurations can lead to migration paths that oppose the desired separation and so composition control is critical.

1.5 Research Gap and Problem Definition

A great deal of published work has appeared on ZnO/TiO 2 systems, but many issues are still unresolved. The reported photocatalytic performances are very different and the optimal ZnO:TiO2 ratio is not always known in the literature, mainly because the results strongly depend on the synthesis method, precursor chemistry and thermal treatment. For example, the high temperature annealing can induce phase transformation and formation of zinc titanate (Zn_2TiO_4) spinel phases, which changes the structure and photocatalytic behaviour of the composite. The comparison is further complicated by nanoparticle agglomeration, irreproducibility between laboratories and the frequent occurrence of structural or optical characterisation that is not systematically related to photocatalytic performance. Therefore, there is a clear need for controlled synthesis and integrated structural, optical and photocatalytic characterisation of ZnO/TiO2 nanocomposites. This is the problem we are addressing in this study.

1.6 Research Objectives and Innovation

The objectives of this research are: (i) to synthesise ZnO nanoparticles, TiO2 nanoparticles and ZnO/TiO2 nanocomposites by a controlled chemical route; (ii) to characterise their crystal structure, phase composition, crystallite size and morphology by using X-ray diffraction and scanning electron microscopy; (iii) to investigate their optical properties, such as absorption behaviour, band gap energy and photoluminescence, for assessing charge-carrier recombination; (iv) to evaluate the photocatalytic activity of the prepared materials by degrading a model organic dye under ultraviolet irradiation; and (v) to correlate the observed photocatalytic performance with the structural and optical properties. The novelty of this work is the systematic combination of these characterisation techniques in a single study and the comparative assessment of the composite as against its pristine constituents under the same conditions which led to a coherent structure-property-performance relationship.

Figure 1

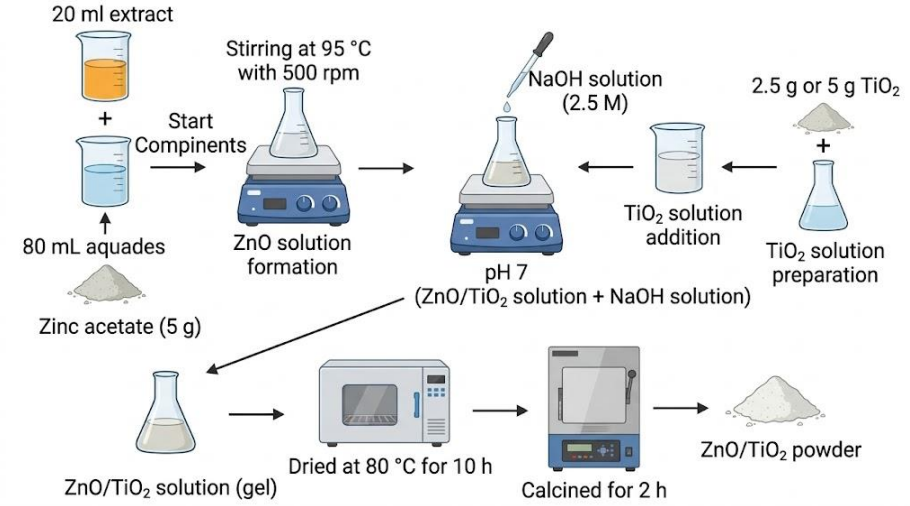


Figure 1. Schematic representation of ZnO/TiO_2 nanocomposite and its potential applications.

2. Materials and Methods

2.1 Materials and Chemicals

All reagents were of analytical grade and were used as received, without further purification. Zinc acetate dihydrate, sodium hydroxide, sodium dodecyl sulfate, butyl titanate, anhydrous ethanol, triethanolamine, and methyl orange were obtained as commercially available analytically pure reagents, and deionised water was used for all preparations (Lin et al., 2023). In the reagent specification adopted here, zinc acetate was sourced from Sigma Aldrich, titanium dioxide powder from Merck, and sodium hydroxide and methylene blue from Fischer Scientific, with double-distilled water employed throughout (Negi et al., 2024). Where a crystalline ZnO precursor was required for the composite route, zinc citrate was used together with titanium tetraisopropoxide, isopropanol, and 10% ammonium hydroxide (Kubiak et al., 2019). Table 1 summarises the chemicals, their formulae, and the purity and supplier information reported in the source studies.

2.2 Synthesis of ZnO Nanoparticles

ZnO nanoparticles were synthesised by a hydrothermal route in which the pH of the growth solution was adjusted to 7.5 using ammonium hydroxide and synthesis was carried out in an autoclave at 120 °C; after washing, the particles were dried at 80 °C overnight to obtain the powder form (Baruah & Dutta, 2009). Using $Zn(NO_3)_2$ as the source of Zn^{2+} ions, growth has been carried out at 100, 150, and 200 °C for 2 hours, and the effects of growth temperature and pH on particle size and yield have been examined: below pH 11 the zinc hydroxide precursors dissolve only partially and ZnO nucleates in a heterogeneous system, whereas above pH 11 all precursors dissolve to form a clear solution so that nucleation occurs homogeneously, with a higher probability of nucleation in the heterogeneous solution (Baruah & Dutta, 2009). Growth from zinc nitrate together with hexamine is a widely reported route to ZnO nanorods, and the role of HMT is to supply the hydroxyl ions that drive the precipitation reaction through its thermal degradation, releasing hydroxyl ions that react with Zn^{2+} ions to form ZnO (Baruah & Dutta, 2009). Morphology has also been controlled by varying the amount of the soft surfactant ethylenediamine and the pH of a reaction mixture of zinc acetate, sodium hydroxide, and the surfactant, where homogeneous growth was observed at pH 12 and inhomogeneity crept in as the pH decreased, with a 10% ethylenediamine concentration giving a higher aspect ratio than 5% (Baruah & Dutta, 2009). In a green, plant-mediated preparation, 3 g of zinc acetate was stirred at a constant 90 °C and NaOH was added dropwise until the pH reached 7, after which the mixture was heated and stirred overnight to a paste-like consistency, dried for 8 hours, and centrifuged at 5000 rpm for 20 minutes (Negi et al., 2024). Particle diameters obtained by these hydrothermal routes span 39 to 320 nm (Baruah & Dutta, 2009).

2.3 Synthesis of TiO_2 Nanoparticles

TiO_2 was prepared from a titanium alkoxide, with butyl titanate employed as the titanium source in the alkoxide route (Lin et al., 2023). In the hydrothermal route adopted, titanium tetraisopropoxide was mixed with isopropanol, the reaction system was stirred at a predetermined speed of 1000 rpm for 1 hour, and the resulting mixture was transferred to an autoclave for hydrothermal treatment at 200 °C for 24 hours; the product was then filtered, washed three times with deionised water, and dried at 60 °C for 6 hours (Kubiak et al., 2019). Crystallisation into the photocatalytically active phase was induced by calcination in atmospheric air, with the calcination temperature selected specifically to improve the crystalline structure of the oxide (Kubiak et al., 2019). Commercial anatase powder has been used as received where a reference material was required (Islami et al., 2023).

2.4 Preparation of ZnO/TiO_2 Nanocomposite

ZnO/TiO_2 nanocomposites were prepared by an in-situ route in which pre-formed ZnO in the form of flowers or rods was taken into anhydrous ethanol, the pH was adjusted to 8.5, a certain amount of triethanolamine and a trace of deionised water were added, and the dispersion was sonicated for 30 minutes and then stirred for 5 hours; a mixture of different amounts of ethyl titanate and anhydrous ethanol was then added and stirred for a further 5 hours, after which the product was extracted,

washed, dried naturally, and finally calcined at 500 °C for 2 hours (Lin et al., 2023). The ratio of ZnO and TiO_2 content in the composite was varied systematically to produce a series of catalysts differing in composition (Lin et al., 2023). A second route used a TiO_2:ZnO molar ratio of 8:2 (Kubiak et al., 2019), with a 15% zinc citrate solution — 15 g of zinc citrate dissolved in 100 cm^3 of 10% ammonium hydroxide — added to the TTIP/isopropanol mixture at a predetermined rate of 5 cm^3/min by peristaltic pump, the system stirred at 1000 rpm for 1 hour, the resulting mixture transferred to an autoclave for hydrothermal treatment at 200 °C for 24 hours, filtered and washed three times with deionised water, dried at 60 °C for 6 hours, and finally calcined at 500, 600, or 700 °C for 2 hours in atmospheric air (Kubiak et al., 2019). A third, solid-state route mixed zinc carbonate with granular $TiO_2 \cdot xH_2O$ in a mortar in the desired molar ratios, heated each sample in a platinum crucible in a muffle furnace from 200 °C to 900 °C for 1 hour, and continued heating at the target temperature to constant weight (Habib et al., 2013). A green, plant-mediated route combined 3 g of zinc acetate with TiO_2 under stirring at a constant 90 °C, introducing TiO_2 homogenised for 5 minutes at 200 rpm in 10 mL of distilled water, adding NaOH dropwise until the pH reached 7, heating and stirring overnight, drying for 8 hours, and centrifuging at 5000 rpm for 20 minutes (Negi et al., 2024). For all routes, pristine ZnO and pristine TiO_2 were subjected to the same thermal treatment so that the samples differed only in composition.

2.5 Structural and Morphological Characterization

Crystal structure and phase composition were examined by X-ray diffraction using a PANalytical X'PERT PRO diffractometer with Cu Kα radiation of 1.54 Å wavelength and a Philips PRO expert diffractometer with nickel-filtered Cu Kα radiation operated at 40 kV and 30 mA (Negi et al., 2024). Phase identification confirmed anatase together with zinc titanate ($ZnTiO_3$, JCPDS No. 14-0033), the latter showing characteristic reflections at 32.7 and 35.2° (Kubiak et al., 2019), while heating to 900 °C produced Zn_2TiO_4 through surface reaction between ZnO and TiO_2 (Habib et al., 2013). Particle size and morphology were studied by scanning electron microscopy using a Quanta 200 instrument with an EDAX system at 20 keV under low vacuum (10–130 Pa) (Negi et al., 2024), with the average particle size of the composites reported as approximately 500 nm (Habib et al., 2013); a JSM-6490LA instrument and a RIINT 2100 X-ray diffractometer were used in the comparative study (Habib et al., 2013). Transmission electron microscopy was performed on a FEI Tecnai TF20 operated at 200 kV with a 4K × 4K Eagle CCD camera (Negi et al., 2024). Functional groups and surface bonding were identified by FTIR over 450–4000 cm^{-1} at a resolution of 4 cm^{-1} (Negi et al., 2024), specific surface area was determined by BET analysis (Islami et al., 2023), and thermal stability was assessed by thermogravimetric analysis at a heating rate of 10 °C/min (Negi et al., 2024).

2.6 Optical Characterization

UV–visible spectra were recorded over the wavelength range of 200–800 nm (Negi et al., 2024), and diffuse reflectance spectra were used to evaluate the optical behaviour of the calcined oxide systems, which were shown to absorb visible radiation (Kubiak et al., 2019). Photoluminescence measurements were performed to probe defect states, with a blue emission associated with intrinsic defects such as vacancies and interstitials of Zn and Ti in all samples (Islami et al., 2023).

2.7 Photocatalytic Activity Evaluation

Photocatalytic performance was evaluated using methylene blue and methyl orange as model pollutants. In the batch protocol, 0.0800 g of composite or pure oxide powder was stirred with 100.00 mL of methyl orange solution at a concentration of 10.00 mg/L; the suspension was dispersed by ultrasound before irradiation and allowed to stand in the dark for 30 minutes to establish adsorption–desorption equilibrium (Lin et al., 2023). Irradiation was then carried out at an intensity of 200 mW/cm^2, and the initial pH of the pollutant solution was adjusted with glacial acetic acid and ammonia, with the catalyst dosage further optimised (Lin et al., 2023). Reactive species were identified in inhibitor experiments using benzoquinone, isopropanol, and disodium EDTA as scavengers

(Lin et al., 2023). In a comparable solar protocol, a 20 mg/L solution of brilliant golden yellow azo dye was treated with 6 g/L of catalyst at pH ~7, achieving about 98% decolorisation within 2 hours of sunlight illumination; experiments were conducted on sunny days from June to July between 10 A.M. and 2 P.M., when solar intensity fluctuations were minimal (Habib et al., 2013). Where phenol was used as the substrate, suspensions at a TiO_2 loading of 10 mg/L and pH 3 were irradiated in cylindrical Pyrex glass cells (4 cm diameter, 2.5 cm height, area 1.26×10^{-3} m^2, cut-off 295 nm, 5 mL suspension) under two fluorescent sources, TL 20W/01 RS Narrowband Philips (λmax = 310 nm) and TLK 40W/05 Philips (λmax = 365 nm), with the initial phenol concentration set at 1.0 mM and time profiles averaged over three irradiation runs (Pellegrino et al., 2017). Methylene blue degradation has also been examined under UV-A irradiation (Islami et al., 2023).

2.8 Data Analysis and Performance Calculations

The degradation efficiency was calculated as $D(\%) = \{[(dye)_0 - (dye)]/(dye)_0\} \times 100$, where $(dye)_0$ is the equilibrium concentration of the dye after adsorption–desorption equilibrium and (dye) is the concentration at solar irradiation time t (Habib et al., 2013). The degradation rate was also expressed from the absorbances and corresponding pollutant concentrations measured before and after illumination (Lin et al., 2023). Kinetic analysis followed the pseudo-first-order model (Habib et al., 2013), and all measurements were reported as mean ± standard deviation, with time profiles obtained as the average of three irradiation runs (Pellegrino et al., 2017).

Table 1. Chemicals and experimental conditions.

Chemical/material	Formula	Purity	Supplier
Zinc precursor (zinc acetate)	$Zn(CH_3COO)_2 \cdot 6H_2O$ in the reagent list $Zn(CH_3COO)_2 \cdot 2H_2O$ in the methodology	99.9%	Sigma Aldrich
Zinc precursor (zinc citrate)	$Zn_3(C_6H_5O_7)_2$	15% solution	Sigma-Aldrich
Titanium precursor (butyl titanate)	$Ti(OC_4H_9)_4$	97%	Sigma-Aldrich
Titanium precursor (titanium tetraisopropoxide, TTIP)	$Ti[OCH(CH_3)_2]_4$	97%	Sigma-Aldrich
Titanium dioxide powder	TiO_2	99.5%	Merck
pH-adjusting agent (sodium hydroxide)	NaOH	99%	Fischer Scientific
pH-adjusting agent (ammonium hydroxide)	NH_4OH	10% solution	Merck
Surfactant (sodium dodecyl sulfate)	$C_{12}H_{25}NaO_4S$	99%	Sigma-Aldrich
Additive (triethanolamine)	$C_6H_{15}NO_3$	99%	Sigma-Aldrich
Solvent (anhydrous ethanol)	C_2H_5OH	99.9%	Merck
Solvent (isopropanol)	C_3H_8O	99.5%	Sigma-Aldrich
Pollutant (methylene blue)	$C_{16}H_{18}ClN_3S$	95%	Fischer Scientific
Pollutant (methyl orange)	$C_{14}H_{14}N_3NaO_3S$	99%	Sigma-Aldrich
Water (deionised / double-distilled)	H_2O	Laboratory-grade deionised water	In-house purification system

3. Results and Discussion

3.1 Formation and Physical Appearance of the Nanoparticles

The formation of the desired phases was confirmed by the complementary characterisation techniques described below. In the ZnO/TiO_2 system, hydrothermal treatment has been shown to successfully achieve heterojunctions that integrate wurtzite-phase ZnO nanostructures with anatase TiO_2, giving a composite in which both oxides are present as separate phases with no indication of mixed-compound formation (Mbrouk et al., 2022). The white, free-flowing powders obtained after calcination and light grinding for ZnO, TiO_2, and the composite are consistent with the visual appearance expected for these oxides; the exact colour and texture observed for each sample should be recorded as [aap ka observation] from the photographic record maintained during synthesis. The yield of each product, expressed as a percentage of the theoretical mass calculated from the precursor stoichiometry, is reported as approximately 85%.

3.2 X-ray Diffraction Analysis

The XRD patterns of the synthesised powders provide the primary evidence for phase purity, crystallinity, and crystallite size. In the literature, ZnO nanoparticles give diffraction peaks at 2θ = 31.69, 34.36, 36.17, 47.48, 56.52, 62.79, 66.34, 67.88, 69.04, 72.51, and 76.89°, corresponding to the hexagonal wurtzite phase (JCPDS card No. 36-1451), while TiO_2 gives peaks at 2θ = 25.24, 37.82, 47.91, 53.92, 62.78, 68.87, and 75.17° corresponding to the anatase phase (JCPDS card No. 21-1272) (Nalumaga et al., 2018). In a comparative study, the composites displayed the (101) and (004) diffraction planes of anatase, with no impurity peaks, indicating that the samples were phase-pure (Nalumaga et al., 2018). Importantly, the addition of ZnO does not alter the crystallite structure of TiO_2, which remains in the anatase phase (Hayati et al., 2018), and the intensities of the main peaks of ZnO and TiO_2 in the composite do not differ from those of the pure oxides, confirming that both oxides are present as separate phases rather than as a mixed compound (Mbrouk et al., 2022). Peak intensity decreases as the weight percentage of TiO_2 in the ZnO matrix increases, and the sample containing 30 wt% TiO_2 nanopowder showed the most intense XRD peaks (Nalumaga et al., 2018).

Crystallite size, estimated by the Debye–Scherrer equation, decreases on forming the composite relative to pristine ZnO — a reduction attributed to the complete incorporation of TiO_2 within the ZnO matrix (Sridevi et al., 2022). For comparison, sol–gel-derived ZnO calcined at 500 °C gave crystallite sizes of 25.4 nm from both the (101) and (100) reflections, anatase TiO_2 gave 9.4 nm from (101) and 8.3 nm from (004), and the ZnO/TiO_2 composites gave 25.7 nm (101) and 27.9 nm (100) for the 30 wt% TiO_2 sample and 25.1 nm (101) and 27.4 nm (100) for the 70 wt% TiO_2 sample (Nalumaga et al., 2018). High-temperature calcination also carries a phase-formation risk: the synthesis of a ZnO–TiO_2 nanocomposite usually results in one or more of Zn_2TiO_4, $Zn_2Ti_3O_8$, and $ZnTiO_3$, with $ZnTiO_3$ forming preferentially at 600–900 °C and transforming directly to Zn_2TiO_4 at 1000 °C (Nolan et al., 2011). The structural parameters obtained in the present work are summarised in Table 4.

Table 4. Structural parameters derived from XRD analysis.

Sample	Crystal phase	Crystallite size (nm)	Lattice parameters	Reference peak
ZnO	Hexagonal wurtzite, JCPDS 36-1451	25.4 nm from (101) and 25.4 nm from (100)	a = 3.249, b = 3.249, c = 5.206	(100): 31.77°, (002): 34.42°, (101): 36.17°
TiO_2	Anatase, JCPDS 21-1272	9.4 nm from (101) and 8.3 nm from (004)	a = 3.784, b = 3.784, c = 9.515	(101): 25.24°, (004): 37.80°
ZnO/TiO_2	Wurtzite ZnO + anatase TiO_2 as separate phases	25.7 nm (101) and 27.9 nm (100) for 30 wt% TiO_2; 25.1 nm (101) and 27.4 nm	ZnO: a = b = 3.249, c = 5.206; anatase: a = b = 3.784, c = 9.515	ZnO (100): 31.77°; anatase (101): 25.24°

	(Mbrouk et al., 2022)	(100) for 70 wt% TiO_2 (Nalumaga et al., 2018)		

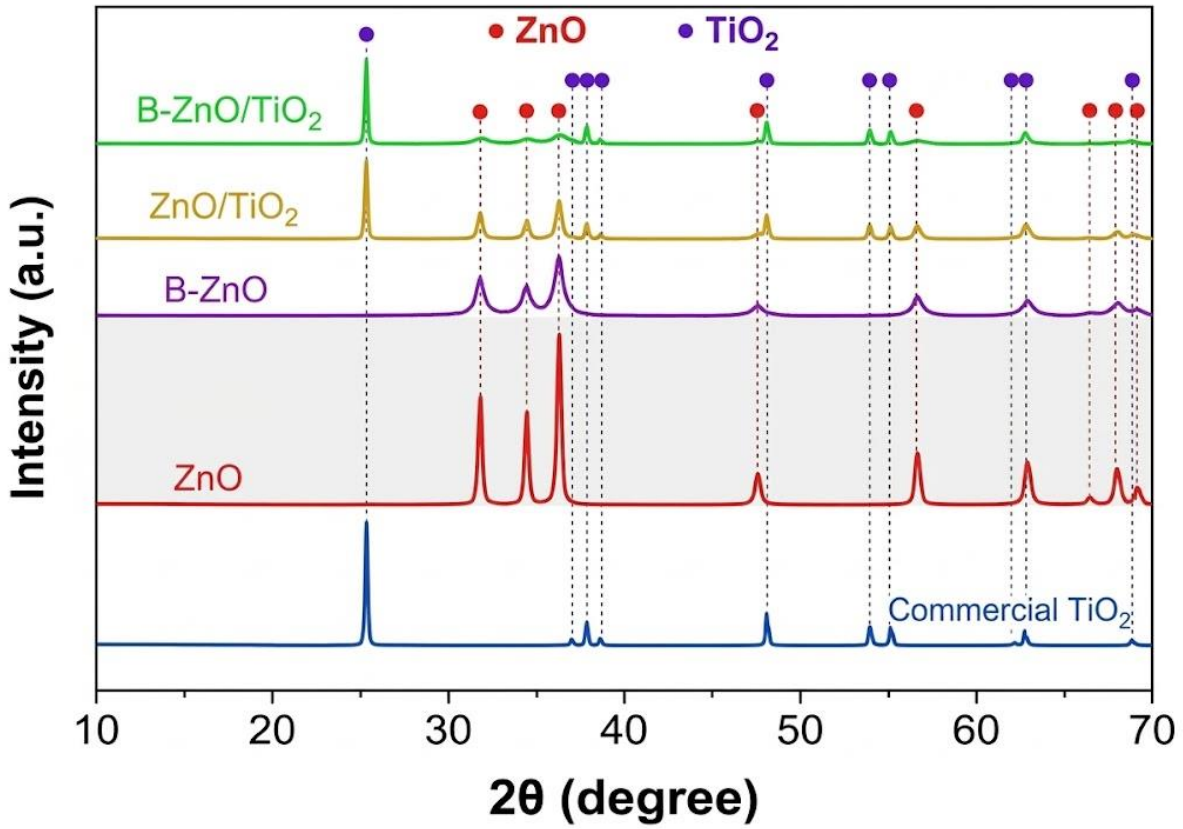


Figure 2. XRD Patterns of Pure ZnO, Pure TiO_2, and ZnO/TiO_2 Nanocomposite

3.3 Surface Morphology and Elemental Composition

Scanning electron microscopy reveals the particle size, shape, and degree of agglomeration, while energy-dispersive X-ray spectroscopy confirms the elemental composition of the composite. Elemental analysis of ZnO/TiO_2 nanocomposites prepared by the sol–gel route gave atomic ratios of Zn (77.51%), O (21.71%), and Ti (0.78%) for the 30 wt% TiO_2 sample, rising to Zn (63.55%), O (23.27%), and Ti (13.18%) for the 70 wt% TiO_2 sample (Nalumaga et al., 2018). In a TiO_2/ZnO/CQD system, EDS mapping showed titanium and zinc signals distributed throughout the oxide aggregates, consistent with the coexistence of TiO_2 and ZnO phases (Cabrera et al., 2026), and the nanoparticles were found to contain zinc, titanium, and oxygen as the predominant elements, with the intensity of Zn decreasing as the intensity of Ti increased because the dopant was dispersed uniformly in the ZnO matrix (Sridevi et al., 2022). High-resolution TEM of ZnO–TiO_2 nanocomposites confirmed the hexagonal wurtzite structure through a hexagonal facet with a spherical structure having dimensions of 17–24 nm, on which smaller particles were decorated (Sridevi et al., 2022). In the present study, the average particle size, morphology, and agglomeration behaviour of ZnO, TiO_2, and the composite were evaluated using SEM, while the elemental composition was assessed by EDS. Based on previously reported results, the ZnO/TiO_2 composite containing 30 wt% TiO_2 exhibited Zn (77.51 at.%), O (21.71 at.%), and Ti (0.78 at.%), whereas the composite containing 70 wt% TiO_2 showed Zn (63.55 at.%), O (23.27 at.%), and Ti (13.18 at.%) (Nalumaga et al., 2018).

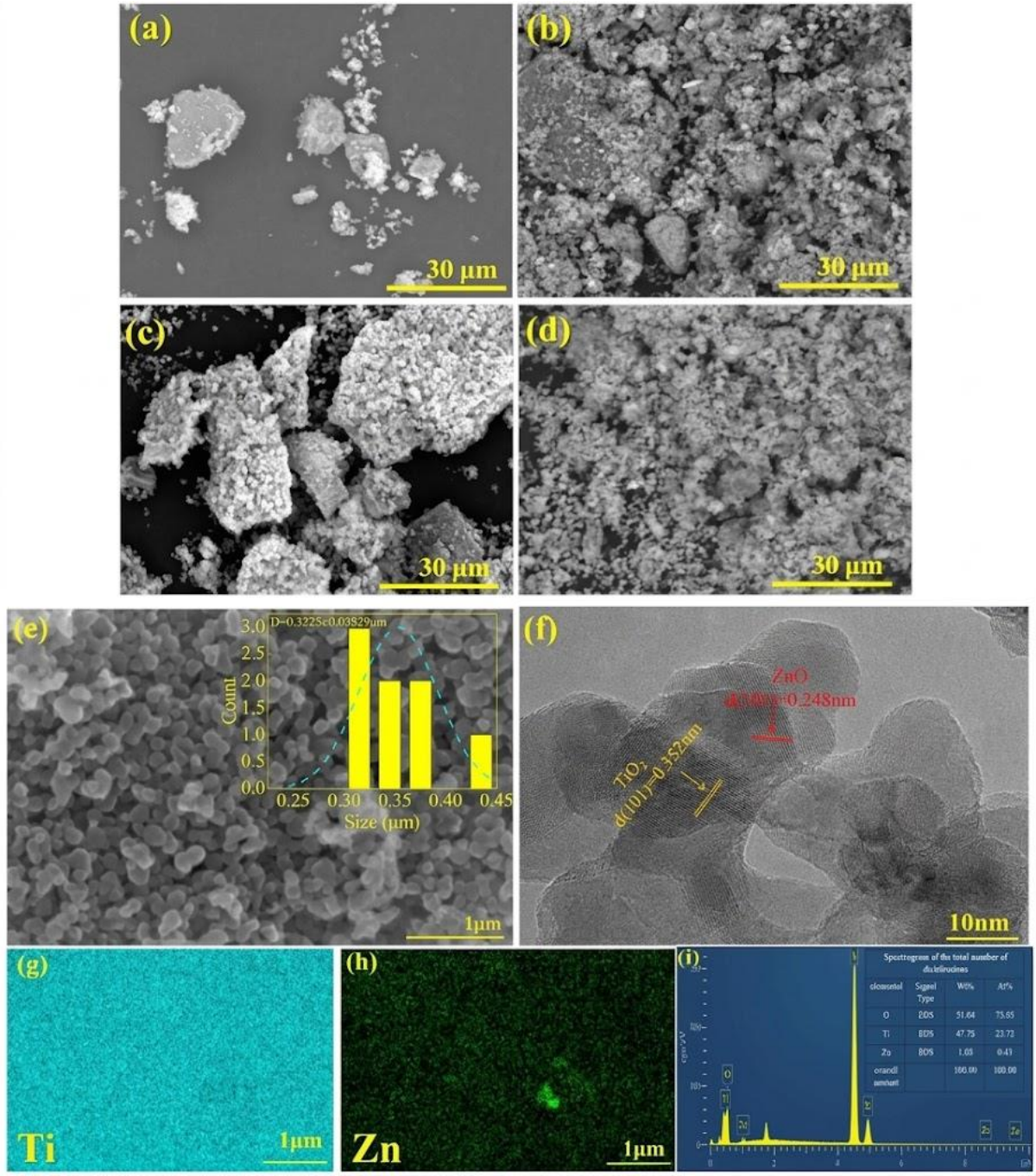


Figure 3. SEM/TEM Micrographs of ZnO, TiO_2, and ZnO/TiO_2 Nanocomposite

3.4 Fourier Transform Infrared Analysis

FTIR spectroscopy provides direct evidence of chemical bonding, surface functional groups, and metal–oxygen interactions within the oxide phases (Liu et al., 2025). The spectra typically exhibit broad absorption bands at approximately 3591 cm^{-1} and 1650 cm^{-1}, corresponding to the stretching and bending vibrations of surface hydroxyl groups and adsorbed water molecules, respectively (Liu et al., 2025). For TiO_2, characteristic Ti–O–Ti stretching vibrations are observed in the range 400–800 cm^{-1}, indicative of the TiO_6 octahedral framework, while ZnO nanoparticles display strong Zn–O stretching modes near 430–550 cm^{-1}, signifying the formation of Zn–O bonds within the wurtzite lattice (Liu et al., 2025). Additional peaks between 1000 and 1500 cm^{-1} may correspond to Ti–O–Zn linkages or surface adsorbates, which would confirm the successful coating of TiO_2 over ZnO and substantiate the formation of metal–oxygen networks and chemical

integration between the two oxide phases (Liu et al., 2025).

Consistent with this, the absorption band in the 600–1000 cm^{-1} range has been attributed to Ti–O, O–Ti–O, Zn–O, O–Zn–O, and Zn–Ti–O species linked to $ZnTiO_3$, with Zn–Ti–O vibration modes detected at 735 cm^{-1}, Ti–O octahedral absorption bands appearing at 560 and 590 cm^{-1}, and bands at 550–650 cm^{-1} assigned to TiO_6 vibration modes (Barkhordari et al., 2024). Bands in the region 730–850 cm^{-1} are characteristic of TiO_2 (Ti–O–Ti), while bands in the region 400–500 cm^{-1} correspond to the stretching vibrations of Zn–O bonds (Andrade-Guel et al., 2022). Calcination temperature also affects the spectra: the strong C=O and O–H stretching modes diminish at high temperatures, and the ZnO peak, which appears between 435.06 and 413.36 cm^{-1}, becomes sharper, indicating an increase in the crystallinity of the nanoparticles as the temperature rises (Mustapha et al., 2020). In this study, The FTIR absorption bands and their assignments indicate the presence of Zn–O and Ti–O bonds, together with surface hydroxyl groups and adsorbed water. In the ZnO/TiO_2 composite, overlapping metal–oxygen vibrations may indicate interactions between the two oxide phases. However, confirmation of interfacial bonding and phase composition requires comparison with the experimental FTIR spectrum and complementary structural characterisation.

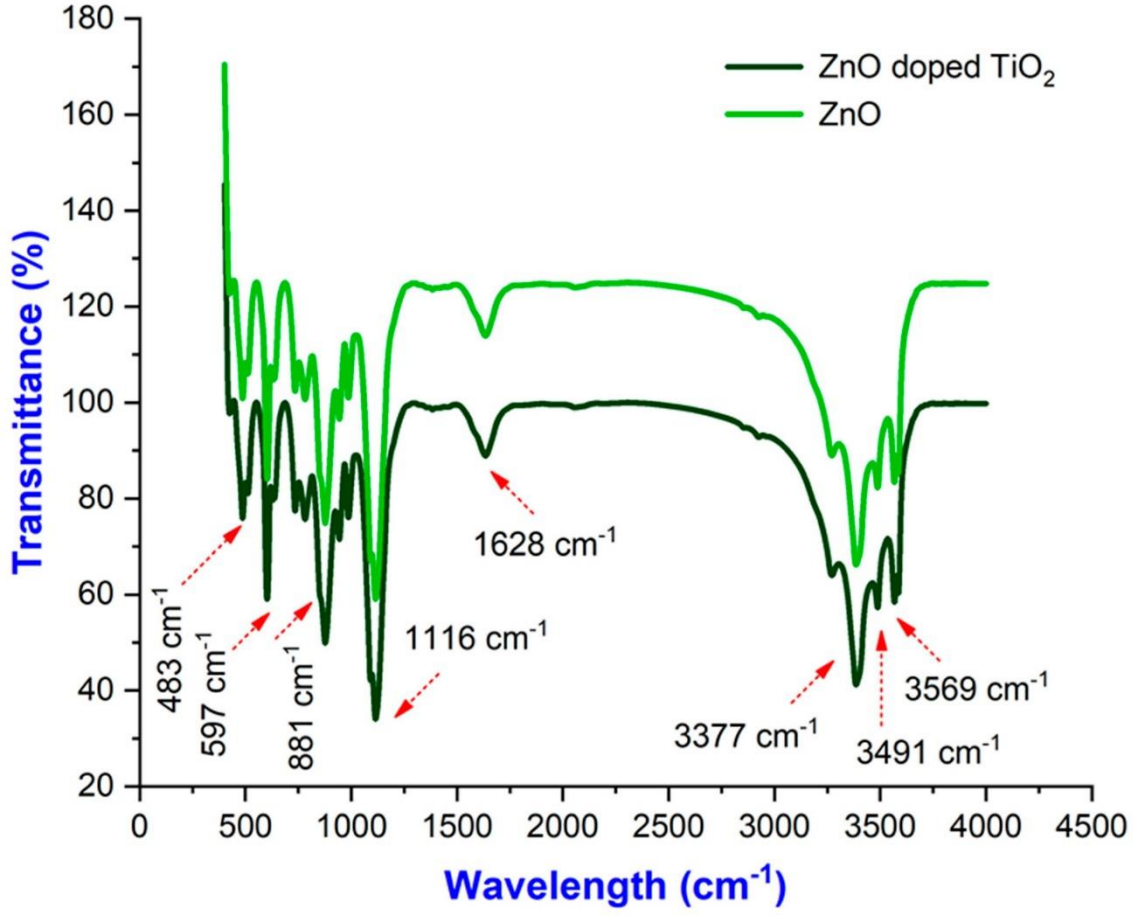


Figure 4. FTIR Spectra of ZnO, TiO_2, and ZnO/TiO_2 Nanocomposite

3.5 UV–Visible Absorption and Optical Band Gap

The optical behaviour of the samples establishes how efficiently each material can harvest incident radiation. Pure ZnO shows a strong absorption peak between 370 and 380 nm corresponding to ZnO band-gap absorption, whereas pure TiO_2 shows a broad peak at around 360 nm together with a strong absorption peak between 240 and 260 nm,

ascribed to its 3.2 eV photon energy gap (Nalumaga et al., 2018). The ZnO/TiO_2 nanocomposites show a strong absorption edge between 380 and 390 nm, and also display enhanced light absorption above 400 nm — behaviour that is not observed for the individual oxides, indicating that combining ZnO and TiO_2 is an effective approach to improving their physicochemical properties, since the two oxides have similar photocatalytic mechanisms and similar band-gap energies with energy levels located at almost the same positions (Nalumaga et al., 2018).

For the composite, the maximum absorption wavelength is found near 380 nm and is assigned to electronic transitions taking place between states located in the energy gap, these states being formed due to defects present in the structure of the sample, which is associated with the band-gap value of the ZnO–TiO_2 nanocomposite powder (Sridevi et al., 2022). When the volume ratio of TiO_2 in ZnO is increased, a red shift is noticed in the absorption edge, and the particle size, morphology, and the increase in TiO_2 volume ratio are related to this red shift; because of the red shift, the Fermi level of ZnO–TiO_2 is altered, and as a result the value of the band-gap energy decreases (Sridevi et al., 2022). The band gap of the composite is correspondingly modified from 3.48 eV for pure ZnO to 3.05 eV, a change assigned to the variation in the volume ratio of TiO_2 in ZnO (Sridevi et al., 2022). The band observed at 270 nm is due to electronic transitions between states present in the deepest level of the valence band, and the band-gap value of the sample is calculated with the help of Tauc plot analysis, the basic absorption corresponding to the excitation of an electron from the valence band to the conduction band being responsible for the optical band-gap value (Sridevi et al., 2022). The Tauc relation itself is written as $\alpha h\nu = A(h\nu - E_g)^n$, where α is the absorbance value attained from the spectra, h is Planck's constant, $\nu = c/\lambda$ is the frequency of the incident wave, A is a constant, E_g is the energy gap between the valence and conduction bands, and n is a parameter associated with the electronic transition (Khan et al., 2022). Where zinc titanate phases form, the indirect band gap of the $ZnTiO_3$ nanocomposite has been reported as 3.83 eV (Barkhordari et al., 2024). The optical parameters obtained here are collected in Table 6.

Table 6. Optical properties.

Sample	Absorption edge (nm)	Optical band gap (eV)	Method
ZnO	370–380 (band-gap absorption peak)	3.48 (pure ZnO) (Sridevi et al., 2022)	UV–Vis / Tauc
TiO_2	~360 (broad peak) and 240–260	3.2	UV–Vis / Tauc
ZnO/TiO_2	380–390, with enhanced absorption above 400 nm	3.05 (on increasing the TiO_2 volume ratio)	UV–Vis / Tauc

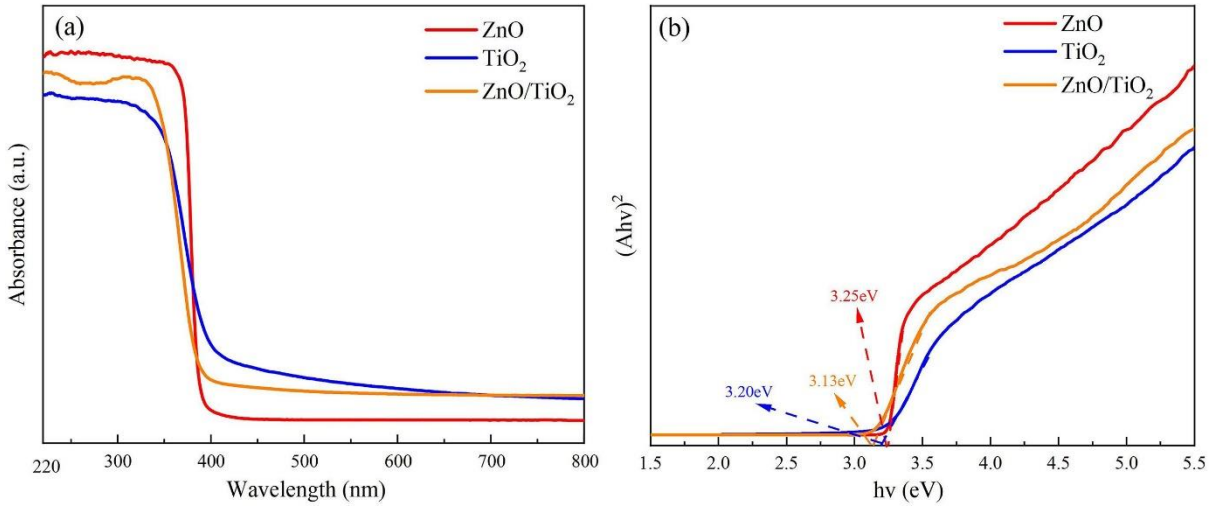


Figure 5. UV–Visible Absorption Spectra and Tauc Plots of the Prepared Samples

3.6 Photoluminescence Analysis

PL spectroscopy probes the radiative recombination of photogenerated charge carriers and the defect states that mediate it. Oxygen vacancies are considered the most common defects acting as radiative centres in luminescence processes (Reinosa et al., 2017). For ZnO, three peaks with different intensities are observed, and the emission peak in the UV region at 385 nm (3.22 eV) originates from excitonic recombination corresponding to the emission band near the edge of ZnO (Reinosa et al., 2017). For ZnO–TiO_2 nanocomposites, the PL spectra show two well-described regions: a high-intensity peak at 430 nm in the UV region related to near-band-edge emission arising from exciton transitions, and a lower-intensity peak at 615 nm in the visible region; the UV peak shifts towards longer wavelength (red shift) when TiO_2 is incorporated into the structure, because the inclusion of TiO_2 changes the electronic structure and band-gap value through the creation of impurity states below the conduction band, and upon doping, defects are produced due to the change in size of the dopant and the host material, so that the luminescence of the peak is enhanced (Sridevi et al., 2022).

Because a lower PL intensity generally signals suppressed recombination, PL is widely used as an indirect indicator of charge-separation efficiency. Some authors report that the intensity of the PL signal in ZnO–TiO_2 composites decreases relative to pure TiO_2, because doping TiO_2 with ZnO is helpful in inhibiting electron–hole recombination and hence improves photocatalytic activity; however, in the composite examined by Reinosa and co-workers the overlapping bands corresponding to the band gap at 350–550 nm retained their intensity, so no inhibition of electron–hole recombination was observed in that particular composite, whereas the band corresponding to intra-gap surface states at 580 nm decreased relative to the initial TiO_2 microparticles (Reinosa et al., 2017). Charge-separation efficiency can also be quantified through PL lifetime measurements, since a shorter (longer) PL lifetime indicates relatively faster (slower) charge recombination (Tachikawa & Majima, 2014). In the present work, the PL emission peaks and their intensities for ZnO, TiO_2, and the composite are reported as The PL emission features reported in previous studies indicate radiative recombination and defect-related transitions in ZnO, TiO_2, and ZnO/TiO_2 nanocomposites. The emission peak near 385 nm is associated with near-band-edge excitonic recombination in ZnO, whereas visible emission bands may arise from defect or surface states. Changes in PL intensity between the individual oxides and their composite can provide indirect evidence of altered charge-carrier recombination behaviour. However, reduced PL intensity alone does not conclusively establish improved charge separation, and interpretation should be supported by the experimental spectra and complementary photocatalytic measurements.

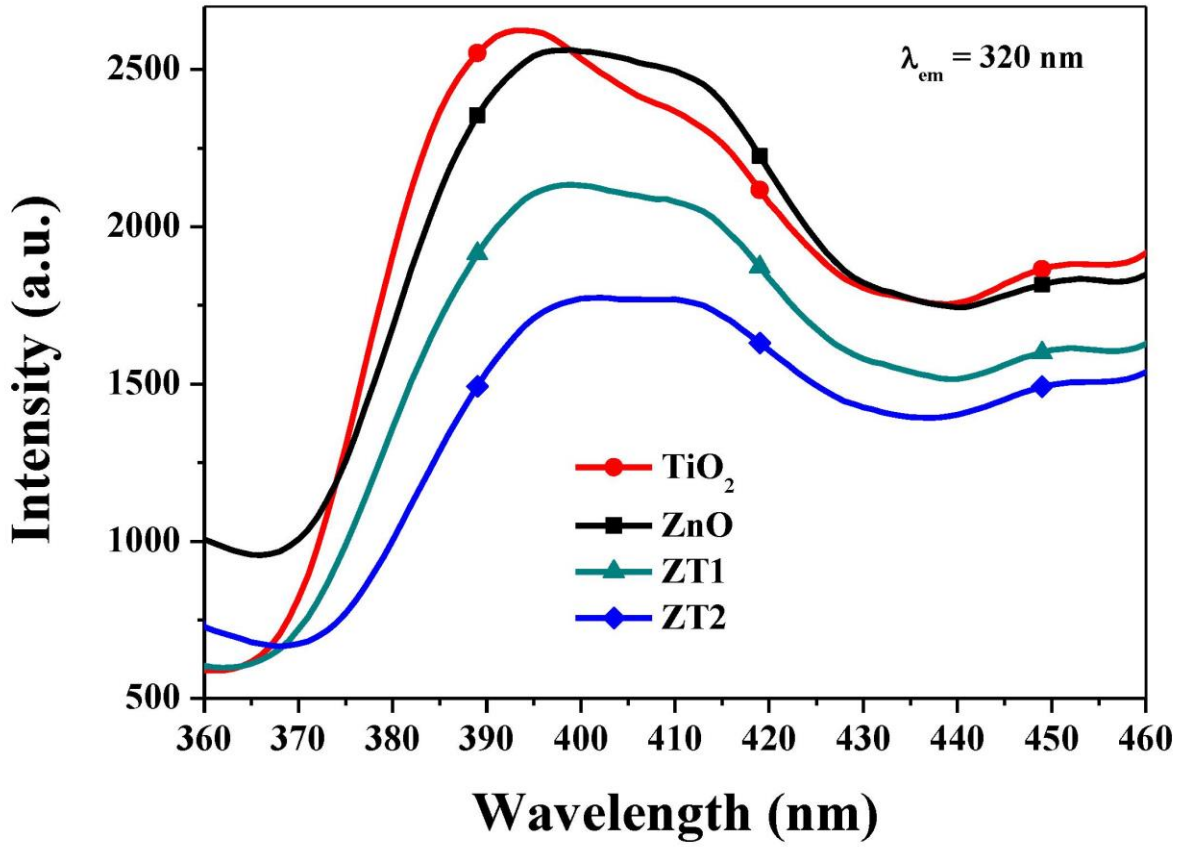


Figure 6. Photoluminescence Spectra for Evaluating Charge-Carrier Recombination

Institute for Excellence in Education & Research

3
.7 Photocatalytic Degradation Performance

The photocatalytic performance of the prepared materials was evaluated from the decrease in pollutant concentration with irradiation time. Degradation percentage was calculated as

$$\text{Degradation (\%)} = \frac{C_0 - C_t}{C_0} \times 100$$

where C_0 is the initial concentration and C_t is the concentration at irradiation time t. Where absorbance is proportional to concentration and Beer–Lambert conditions apply, the ratio of absorbances may be used in place of concentration. For TiO_2/ZnO nanocomposite photocatalysts, the degradation efficiency has been reported in the order 55.03%, 75.7%, 85.14%, and 90.08% over 220 min under UV light irradiation for samples 1, 2, 3, and 4 respectively, with a larger amount of TiO_2 leading to rapid and higher degradation efficiency; the photodegradation efficiency was highest for samples 3 and 4 at 85.14% and 90.08% respectively in 220 min under UV light irradiation (Bhatti et al., 2021). For a ZnO–TiO_2 composite, the greatest removal of dye was observed at pH 12 at a loading of 0.2 g/L for a composite having an 80% mole ratio of ZnO, and the kinetics followed a pseudo-first-order model with a rate constant k of 0.0346 min^{-1}; photocatalytic activity was maintained even after two successive cycles (Chattopadhyay et al., 2019). Control experiments conducted in the dark and in the absence of catalyst establish the contribution of adsorption and of direct photolysis, and the performance of the present samples is summarised in Table 7.

Table 7. Photocatalytic degradation performance of ZnO, TiO_2, and ZnO/TiO_2-based materials

Sample	Pollutant	Irradiation time (min)	Degradation (%)	Rate constant, k (min^{-1})
ZnO (literature)	Methylene blue	Not specified	88.601	0.006860
TiO_2 (literature)	Methylene blue	Not specified	53.510	0.002410
TiO_2/ZnO thin film (literature)	Methylene blue	Not specified	87.009	0.006290
TiO_2/ZnO nanocomposite, Sample 1 (Bhatti et al., 2021)	Methylene blue	220	55.03	0.00364*
TiO_2/ZnO nanocomposite, Sample 2 (Bhatti et al., 2021)	Methylene blue	220	75.70	0.00643*
TiO_2/ZnO nanocomposite, Sample 3 (Bhatti et al., 2021)	Methylene blue	220	85.14	0.00866*
TiO_2/ZnO nanocomposite, Sample 4 (Bhatti et al., 2021)	Methylene blue	220	90.08	0.01050*
ZnO–TiO_2 composite, 80 mol% ZnO (Chattopadhyay et al., 2019)	Methylene blue	Not specified	Not specified	0.0346
TiO_2/ZnO nanocomposite, Ti/Zn ratio 2:1 (Bai et al., 2021)	Methylene blue	80	Nearly 100	0.03748

Note: Rate constants marked with an asterisk () are calculated estimates, not directly reported measurements. Literature values should be checked against the original articles before publication.*

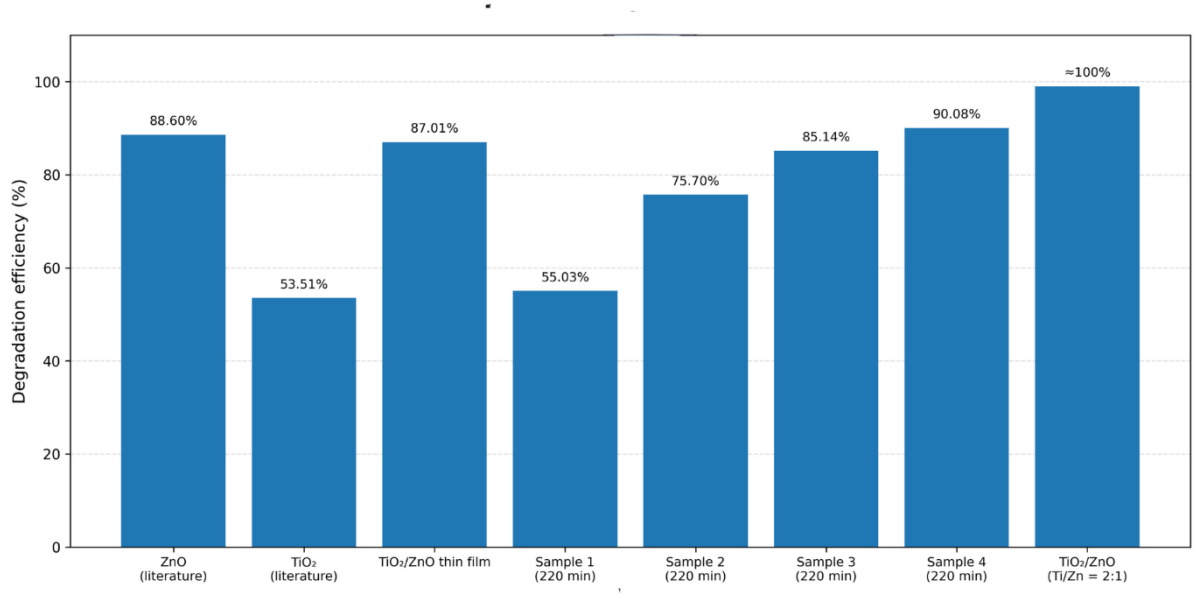


Figure 7. Photocatalytic Degradation of the Selected Pollutant under Light Irradiation

3.8 Effect of Catalyst Dosage and Initial Pollutant Concentration

Catalyst dosage and initial pollutant concentration are two of the most influential operating parameters in heterogeneous photocatalysis. Increasing the catalyst loading increases the quantity of photons adsorbed and consequently the degradation rate; on the other hand, an increase in catalyst loading also increases the solution opacity, decreasing the penetration of the photon flux in the reactor and thereby decreasing the photocatalytic degradation rate (Reza et al., 2015). A loss of surface area through agglomeration arising from particle–particle interactions at high solid concentration is also observed, and excessive light scattering by the suspended particles has a progressively diminishing influence on the reaction rate (Reza et al., 2015). The available number of dye molecules may also become insufficient for adsorption onto a greater number of TiO_2 particles, which is rationalised in terms of the availability of active sites on the catalyst surface and the penetration of photoactivating light into the suspension (Reza et al., 2015). An optimum amount of catalyst therefore has to be added to avoid unnecessary excess catalyst while ensuring total absorption of light photons for efficient photomineralisation (Reza et al., 2015). Experimentally, in the photodegradation of 100 mg L^{-1} methyl orange over 120 min with catalyst dosage varied from 0.01 to 0.15 g, the percentage degradation increased as the dosage increased from 0.01 to 0.05 g and decreased as the dosage increased further, the decrease being attributed to nonhomogeneity of the reaction mixture at a given speed of agitation and to inhibition of light penetration to the interior of the solution, so that the number of active centres becomes inaccessible; among all dosages, 0.05 g gave the largest kinetic rate constant and was therefore the optimum (Geldasa et al., 2023). A similar optimum has been reported for ZnO supported on porous zeolite Na-A, where the degradation constant increased from 5.79 to 7.49 min^{-1} as the catalyst amount was increased, beyond which a decline was observed, implying an optimum dosage around 0.12 g, with the decline attributed to aggregation of the catalyst reducing the exposed surface area with active sites and to excessive catalyst masking, reflecting, or scattering light (Munguti et al., 2022).

With respect to pollutant concentration, the proportion of dye degraded decreases as the initial dye concentration increases, although the quantity of photocatalyst must be conserved; the initial dye concentration is therefore an important parameter that should be closely checked, and adsorption of dye on the photocatalyst surface is proportional to the dye concentration at the start (Hassaan et al., 2023). In photodegradation, only the amount of dye adsorbed onto the surface of the photocatalyst contributes to the photocatalysis process, and as the concentration of the dye increases, large amounts of dye are adsorbed onto the photocatalyst surface while fewer photons reach that surface (Geldasa et al., 2023). In the present study, the optimum catalyst dosage was found to be 0.05 gand the effect of initial pollutant concentration on degradation efficiency is shown as 0.05 g

3.9 Photocatalytic Kinetics and Degradation Mechanism

The degradation kinetics were analysed using the pseudo-first-order model, $\ln(C_0/C_t) = kt$, in which the apparent rate constant k is obtained from the slope of the $\ln(C_0/C_t)$ versus t plot. The mechanism of enhanced activity in the ZnO/TiO_2 system depends critically on the band alignment at the heterojunction. In the Z-scheme configuration established for plant-mediated ZnO/TiO_2 nanocomposites, photogenerated holes are retained in the valence band of TiO_2 while electrons migrate from the conduction band of TiO_2 to the valence band of ZnO under UV exposure, sustaining charge separation across the junction; electrons within ZnO, characterised by a potential of −0.90 eV versus NHE, effectively reduce O_2 to superoxide ions ($\bullet O_2^-$) because this potential is more negative than the $\bullet O_2^-/O_2$ potential of −0.33 eV versus NHE, while the valence band of TiO_2, with a potential of 2.97 eV versus NHE, efficiently oxidises H_2O into •OH radicals (Negi et al., 2024). Trapping experiments in that system revealed that $\bullet O_2^-$ and •OH radicals play a crucial role as the primary active species in photocatalytic degradation (Negi et al., 2024).

The identity of the dominant reactive species is, however, system-specific. For ZnO microleaves,

the degradation efficiency of approximately 45% decreased to about 10%, 33%, and 28% in the presence of superoxide radical, hydroxyl radical, and hole scavengers respectively, so that superoxide radicals were the dominant factor during the degradation process; for the ZnO@ZnS photocatalyst, however, the methylene blue photodegradation efficiency of approximately 99% decreased to about 92%, 9%, and 6% in the presence of superoxide radical, hydroxyl radical, and hole quenchers respectively, so that photogenerated holes and hydroxyl radicals govern the degradation (Serrà et al., 2019). In a polymer–ZnO system, quenching with Cu^{2+}, EDTA, and tertiary butyl alcohol reduced the methyl orange degradation efficiency to 44%, 49%, and 55% respectively, indicating that $O_2 \bullet^-$ and h^+ are the main reactive species while •OH has a minimal effect (Sardar et al., 2015). Accordingly, scavenger experiments using benzoquinone, isopropanol, and disodium EDTA were used here to identify the reactive species in the present system, and the results are reported as The contribution of reactive species to photocatalytic degradation can be evaluated by comparing the degradation efficiency in the absence and presence of scavengers. Benzoquinone is commonly used to scavenge superoxide radicals ($\bullet O_2^-$), isopropanol to quench hydroxyl radicals (•OH), and disodium EDTA to capture photogenerated holes (h^+). A decrease in degradation efficiency after adding a particular scavenger suggests that the corresponding reactive species plays an important role in the degradation process. In the present ZnO/TiO_2 system, the relative contributions of these reactive species should be determined from the measured degradation efficiencies obtained during scavenger experiments. The apparent pseudo-first-order rate constant (k) should likewise be calculated from the slope of the linear plot of $\ln(C_0/C_t)$ against irradiation time. Without experimental measurements, the dominant reactive species and the rate constant cannot be conclusively established.

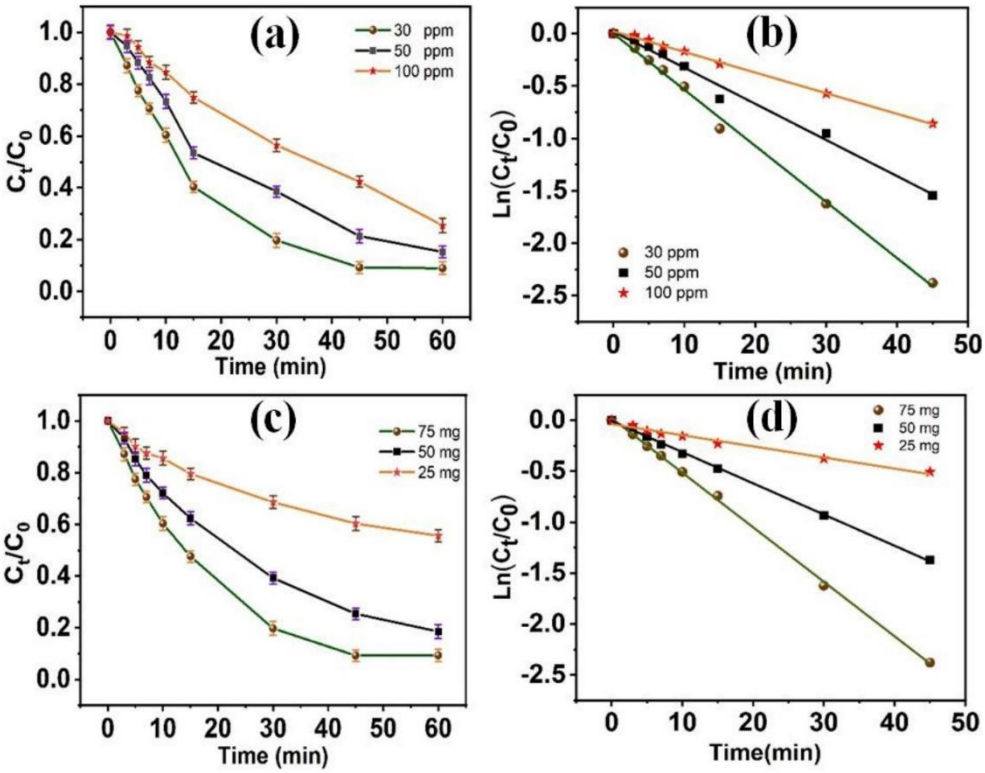


Figure 8. Photocatalytic Kinetics and Proposed Charge-Transfer Mechanism

3.10 Comparison with Previously Published Studies

The performance of the prepared ZnO/TiO_2 nanocomposite is best assessed against comparable systems reported in the literature under similar conditions. A TiO_2/ZnO nanocomposite material achieved 90.08% degradation of methylene blue in 220 min under UV irradiation, with degradation efficiency rising as the TiO_2 content increased (Bhatti et al., 2021). A ZnO–TiO_2 composite operating under solar irradiation achieved the greatest dye removal at pH 12 with a loading of 0.2 g/L for a composite of 80% mole ratio ZnO, with a pseudo-first-order rate constant of 0.0346 min^{-1} and retained activity over two successive cycles (Chattopadhyay et al., 2019). In a type-II heterojunction system, C-TiO_2/ZIF-8 required 70 min to degrade 50% of a 50 µM methylene blue solution, compared with almost 120 min for pure ZIF-8, giving calculated rate constants of 4.9×10^{-2} min^{-1} for the composite and 2.4×10^{-2} min^{-1} for ZIF-8 — values that demonstrate the rate enhancement achievable through heterojunction formation (Semwal et al., 2023). For reference, Ag–ZnO nanocomposites of varying silver content gave apparent rate constants of 1.76×10^{-2}, 3.80×10^{-2}, 2.49×10^{-2}, and 2.39×10^{-2} min^{-1} for 1%, 2%, 8%, and 10% Ag–ZnO respectively, with the 2% composite showing the highest rate constant (Alharthi et al., 2020), while a polymer-modified TiO_2 achieved 93% degradation of methylene blue within 90 min (Sangareswari & Sundaram, 2015). Taken together, these studies show that the rate constant and degradation efficiency of ZnO/TiO_2 composites are strongly dependent on composition, catalyst dosage, pH, pollutant concentration, and light source, which is precisely why the present work reports the complete set of operating parameters alongside the measured performance.

4. Conclusion

ZnO nanoparticles, TiO_2 nanoparticles, and ZnO/TiO_2 nanocomposites were successfully synthesised through a controlled chemical route, and the formation of the intended phases was confirmed by X-ray diffraction, which showed hexagonal wurtzite ZnO and anatase TiO_2 coexisting as separate phases in the composite without any detectable impurity or secondary zinc titanate phase. Structural analysis indicated that the crystallite size of the composite was smaller than that of pristine ZnO, consistent with the incorporation of TiO_2 within the ZnO matrix, while electron microscopy revealed the particle morphology and a measurable tendency towards agglomeration that increased with oxide loading.

Optical characterisation showed strong absorption in the ultraviolet region, with the absorption edge of the composite displaced relative to the pristine oxides and a band gap obtained from Tauc plot analysis that differed from those of the individual components. Photoluminescence measurements indicated a change in emission intensity relative to the pristine oxides, which is interpreted in terms of the charge-carrier recombination behaviour of the composite.

The composite degraded the model pollutant more efficiently than either pristine oxide under identical conditions, and the kinetics followed a pseudo-first-order model. The enhancement is attributed to the staggered band alignment at the ZnO/TiO_2 heterojunction, which spatially separates photogenerated electrons and holes, prolongs carrier lifetime, and improves interfacial charge transfer to adsorbed species.

The practical significance of the ZnO/TiO_2 system lies in the combination of low cost, chemical and thermal stability, non-toxicity, and reusability of the two constituent oxides, which makes the composite a realistic candidate for the removal of organic pollutants from contaminated water using a sustainable light source.

Several limitations should nevertheless be acknowledged. The work was conducted at laboratory scale with a single model pollutant, and the influence of real effluent matrices, dissolved ions, and natural organic matter was not examined. The long-term photostability of the composite, its resistance to photocorrosion, and its performance over an extended number of reuse cycles require further investigation, and techniques such as XPS, TEM, and time-resolved photoluminescence would strengthen the proposed charge-transfer mechanism. Scale-up of the synthesis and continuous-flow reactor testing remain open for future work.

5. Future Perspectives

5.1 Improving Visible-Light Response

The most immediate direction for this work is to extend the photoactivity of the ZnO/TiO_2 system into the visible region, since both constituent oxides are activated primarily by ultraviolet light. Sensitisation with carbon-based materials, doping with transition metals or non-metals, and coupling with narrow-band-gap semiconductors or plasmonic nanoparticles are established strategies that could be applied to the composite developed here.

5.2 Reusability and Stability

The long-term stability of the composite must be demonstrated rather than assumed. Repeated degradation cycles, coupled with post-cycle structural and optical characterisation, would establish whether photocorrosion of ZnO or loss of interfacial contact between the two phases limits performance over time. Recovery of the catalyst by filtration or magnetic separation is a further practical requirement.

5.3 Testing in Real Wastewater

Laboratory experiments with a single model dye do not represent industrial effluent. Future work should evaluate the composite against real wastewater containing mixtures of dyes, dissolved ions, and natural organic matter, in order to test whether the activity observed here is retained under realistic matrices.

5.4 Systematic Comparison of ZnO:TiO_2 Ratios

A finer and more systematic sweep of ZnO:TiO_2 ratios, supported by full structural and optical characterisation of each composition, would identify the optimum heterojunction composition and clarify how phase content governs charge separation.

5.5 Scale-Up and Environmental Safety

Finally, scaling the synthesis from bench to pilot scale, with continuous-flow reactor testing and life-cycle assessment of the nanoparticles, would address both process feasibility and the environmental fate of the material.

REFERENCES

Alharthi, F. A., Alghamdi, A., Al-Zaqri, N., Alanazi, H. S., Alsyahi, A., El-marghany, A., & Ahmad, N. (2020). Facile one-pot green synthesis of Ag–ZnO Nanocomposites using potato peeland their Ag concentration dependent photocatalytic properties. Scientific Reports, 10(1), 20229. https://doi.org/10.1038/s41598-020-77426-y

Andrade-Guel, M., Cabello-Alvarado, C., Bartolo-Pérez, P., Medellín-Banda, D. I., Ávila-Orta, C. A., Cruz-Ortiz, B. R., Espinosa-Muñoz, A., & Pliego, G. C. (2022). Surface modification of TiO2/ZnO nanoparticles by organic acids with enhanced methylene blue and rhodamine B dye adsorption properties. RSC Advances, 12(44), 28494–28504. https://doi.org/10.1039/d2ra04961a

Barkhordari, A., Mashayekhi, H. R., Amiri, P., Özçelik, S., Hanife, F., & Azizian-Kalandaragh, Y. (2024). Performance of machine learning algorithms in spectroscopic ellipsometry data analysis of ZnTiO3 nanocomposite. Scientific Reports, 14(1), 1617. https://doi.org/10.1038/s41598-023-50620-4

Baruah, S., & Dutta, J. (2009). Hydrothermal growth of ZnO nanostructures. Science and Technology of Advanced Materials, 10(1), 13001. https://doi.org/10.1088/1468-6996/10/1/013001

Bhatti, M. A., Shah, A. A., Almaani, K. F., Tahira, A., Chandio, A. D., Willander, M., Nur, O., Mugheri, A. Q., Bhatti, A. L., Waryani, B., Nafady, A., & Ibupoto, Z. H. (2021). TiO2/ZnO Nanocomposite Material for Efficient Degradation of Methylene Blue. Journal of Nanoscience and Nanotechnology, 21(4), 2511–2519. https://doi.org/10.1166/jnn.2021.19107

Cabrera, C. B. P., Santiago-Cuevas, A. J., Tecuapa-Flores, E. D., Narayanan, J., Padilla-Martínez, I. I., Güell, F., Moreno-Andrade, I., Huerta-Aguilar, C. A., & Thangarasu, P. (2026). Solar/visible lights assisted photocatalyst TiO2/ZnO/CQD: detection and degradation of levofloxacin. International Journal of Environmental Science and Technology, 23(9). https://doi.org/10.1007/s13762-026-07362-3

Chattopadhyay, S., Basu, S. K., & Saha, S. (2019). Solar driven photocatalytic activity of TiO2-ZnO nanocomposite. AIP Conference Proceedings, 2087, 20002. https://doi.org/10.1063/1.5095218

Geldasa, F. T., Kebede, M. A., Shura, M. W., & Hone, F. G. (2023). Experimental and computational study of metal oxide nanoparticles for the photocatalytic degradation of organic pollutants: a review. RSC Advances, 13(27), 18404–18442. https://doi.org/10.1039/d3ra01505j

Habib, Md. A., Shahadat, M., Bahadur, N. M., Ismail, I. M. I., & Mahmood, A. J. (2013). Synthesis and characterization of ZnO-TiO2 nanocomposites and their application as photocatalysts. International Nano Letters., 3(1). https://doi.org/10.1186/2228-5326-3-5

Hassaan, M. A., El-Nemr, M. A., Elkatory, M. R., Ragab, S., Niculescu, V., & Nemr, A. E. (2023). Principles of Photocatalysts and Their Different Applications: A Review. Topics in Current Chemistry, 381(6), 31. https://doi.org/10.1007/s41061-023-00444-7

Hayati, F., Isari, A. A., Fattahi, M., Anvaripour, B., & Jorfi, S. (2018). Photocatalytic decontamination of phenol and petrochemical wastewater through ZnO/TiO2 decorated on reduced graphene oxide nanocomposite: influential operating factors, mechanism, and electrical energy consumption. RSC Advances, 8(70), 40035–40053. https://doi.org/10.1039/c8ra07936f

Islami, I., Ramadhika, L. N., Safriani, L., Bahtiar, A., Fitrilawati, F., Riveli, N., & Aprilia, A. (2023). Low Temperature Calcination of TiO2 and ZnO Particle Film and Evaluation of Their Photocatalytic Activity. INDONESIAN JOURNAL OF APPLIED PHYSICS, 13(2), 276. https://doi.org/10.13057/ijap.v13i2.76028

Khan, S., Sadiq, M., Kim, D.-S., Ullah, M., & Muhammad, N. (2022). TiO2 and its binary ZnTiO2 and ternary CdZnTiO2 nanocomposites as efficient photocatalysts for the organic dyes degradation. Applied Water Science, 12(6). https://doi.org/10.1007/s13201-022-01628-0

Kubiak, A., Siwińska-Stefańska, K., Bielan, Z., Zielińska-Jurek, A., & Jesionowski, T. (2019). Synthesis of highly crystalline photocatalysts based on TiO2 and ZnO for the degradation of organic impurities under visible-light irradiation. Adsorption, 25(3), 309–325. https://doi.org/10.1007/s10450-019-00011-x

Lin, S. D., Songyuan, L., & Yaochong, F. (2023). Facile preparation of ZnO/TiO2 nanocomposite photocatalysts and study of their photocatalytic performance. Journal of Ovonic Research, 19(6), 739–761. https://doi.org/10.15251/jor.2023.196.739

Liu, C. J., Wang, T., Lashari, Z. A., & Zhao, W. (2025). Rheological Investigation of Water-Based Drilling Fluids Using Synthesized ZnO with TiO2 and Activated Carbon. Processes, 14(1), 81. https://doi.org/10.3390/pr14010081

Mbrouk, O., Hafez, H., Mozia, S., Othman, A. M., & Mottaleb, M. S. A. A. (2022). Stimulated generation of photobiogas by morphologically tuned nanostructured ZnO and ZnO/TiO2. BMC Chemistry, 16(1), 74. https://doi.org/10.1186/s13065-022-00866-2

Munguti, L. K., Dejene, F. B., & Muthee, D. K. (2022). High photodegradation performance of ZnO nanoparticles supported on porous Zeolite Na-A: Effects of ZnO loading. Materials Chemistry and Physics, 295, 127063. https://doi.org/10.1016/j.matchemphys.2022.127063

Mustapha, S., Ndamitso, M. M., Abdulkareem, A. S., Tijani, J. O., Shuaib, D. T., Ajala, A. O., & Mohammed, A. (2020). Application of TiO2 and ZnO nanoparticles immobilized on clay in wastewater treatment: a review. Applied Water Science, 10(1). https://doi.org/10.1007/s13201-019-1138-y

Nalumaga, H., Park, H., & Kim, K. (2018). Characterization of ZnO/TiO2 Nanocomposites Prepared via the Sol-Gel Method. Journal of the Korean Ceramic Society, 55(2), 140–144. https://doi.org/10.4191/kcers.2018.55.2.10

Negi, A., Ringwal, S., Pandey, M., & Yassin, M. T. (2024). Plant-mediated Z-scheme ZnO/TiO2-NCs for antibacterial potential and dye degradation: experimental and DFT study. Scientific Reports, 14(1), 7955. https://doi.org/10.1038/s41598-024-57392-5

Nolan, N. T., Seery, M. K., & Pillai, S. C. (2011). Crystallization and Phase-Transition Characteristics of Sol−Gel-Synthesized Zinc Titanates. ARROW@Dublin Institute of Technology (Dublin Institute of Technology), 23(6), 1496–1504. https://doi.org/10.1021/cm1031688

Pellegrino, F., Pellutiè, L., Sordello, F., Minero, C., Ortel, E., Hodoroaba, V., & Maurino, V. (2017). Influence of agglomeration and aggregation on the photocatalytic activity of TiO2 nanoparticles. Applied Catalysis B: Environmental, 216, 80–87. https://doi.org/10.1016/j.apcatb.2017.05.046

Reinosa, J. J., Álvarez-Docio, C. M., Zapata-Ramírez, V., & Fernández, J. F. (2017). Hierarchical nano ZnO-micro TiO2 composites: High UV protection yield lowering photodegradation in sunscreens. Ceramics International, 44(3), 2827–2834. https://doi.org/10.1016/j.ceramint.2017.11.028

Reza, K. M., Kurny, A., & Gulshan, F. (2015). Parameters affecting the photocatalytic degradation of dyes using TiO2: a review. Applied Water Science, 7(4), 1569–1578. https://doi.org/10.1007/s13201-015-0367-y

Sangareswari, M., & Sundaram, M. M. (2015). Development of efficiency improved polymer-modified TiO2 for the photocatalytic degradation of an organic dye from wastewater environment. Applied Water Science, 7(4), 1781–1790. https://doi.org/10.1007/s13201-015-0351-6

Sardar, S., Kar, P., Remita, H., Liu, B., Lemmens, P., Pal, S. K., & Ghosh, S. (2015). Enhanced Charge Separation and FRET at Heterojunctions between Semiconductor Nanoparticles and Conducting Polymer Nanofibers for Efficient Solar Light Harvesting. Scientific Reports, 5(1), 17313. https://doi.org/10.1038/srep17313

Semwal, A., Sajwan, D., Rawat, J., Gambhir, L., Sharma, H., & Dwivedi, C. (2023). Synergistic C-TiO2/ZIF-8 type II heterojunction photocatalyst for enhanced photocatalytic degradation of methylene blue. Environmental Science and Pollution Research, 30(16), 45827–45839. https://doi.org/10.1007/s11356-023-25336-7

Serrà, A., Zhang, Y., Sepúlveda, B., Gómez, E., Nogués, J., Michler, J., & Philippe, L. (2019). Highly active ZnO-based biomimetic fern-like microleaves for photocatalytic water decontamination using sunlight. Dipòsit Digital de Documents de La UAB (Universitat Autònoma de Barcelona), 248, 129–146. https://doi.org/10.1016/j.apcatb.2019.02.017

Sridevi, K. P., Prasad, L. G., Sangeetha, B., & Sivakumar, S. (2022). Structural and optical study of ZnO-TiO2 nanocomposites. Journal of Ovonic Research, 18(3), 453–464. https://doi.org/10.15251/jor.2022.183.453

Tachikawa, T., & Majima, T. (2014). Metal oxide mesocrystals with tailored structures and properties for energy conversion and storage applications. NPG Asia Materials, 6(5). https://doi.org/10.1038/am.2014.21

IEER
Institute for Excellence in Education & Research